# The γ-ray angular distribution in fast neutron inelastic scattering from iron

Beyer, R.; Dietz, M.; Bemmerer, D.; Junghans, A. R.; Kögler, T.; Massarczyk, R.; Müller, S.; Schmidt, K.; Schwengner, R.; Szücs, T.; Takacs, M. P.; Wagner, A.;

Originally published:

April 2018

**European Physical Journal A 54(2018), 58**

DOI: https://doi.org/10.1140/epja/i2018-12492-7

**EPJ manuscript No.**
(will be inserted by the editor)

# The $\gamma$-ray angular distribution in fast neutron inelastic scattering from iron

Roland Beyer[1,a], Mirco Dietz[1,2,b], Daniel Bemmerer[1], Arnd R. Junghans[1], Toni Kögler[1,2], Ralph Massarczyk[1,2,c], Stefan Müller[1], Konrad Schmidt[1,2,d], Ronald Schwengner[1], Tamás Szücs[1], Marcell P. Takács[1], and Andreas Wagner[1]

[1] Helmholtz-Zentrum Dresden - Rossendorf, Bautzner Landstr. 400, 01328 Dresden, Germany
[2] Technische Universität Dresden, 01062 Dresden, Germany

Received: date / Revised version: date

**Abstract.** The angular distribution of $\gamma$-rays emitted after inelastic scattering of fast neutrons from iron was determined at the *n*ELBE neutron time-of-flight facility. An iron sample of natural isotopic composition was irradiated by a continuous photo-neutron spectrum in the energy range from about 0.1 up to 10 MeV. The de-excitation $\gamma$-rays of the four lowest excited states of $^{56}$Fe and the first excited state of $^{54}$Fe were detected using a setup of five high-purity germanium (HPGe) detectors and five $LaBr_3$ scintillation detectors positioned around the sample at 30°, 55°, 90°, 125° and 150° with respect to the incoming neutron beam. The resulting angular distributions were fitted by Legendre polynomials up to $4^{\text{th}}$ order and the angular distribution coefficients $a_2$ and $a_4$ were extracted. The angular distribution coefficients of three transitions in $^{56}$Fe are reported here for the first time. The results are applied to a previous measurement of the inelastic scattering cross section determined using a single HPGe detector positioned at 125°. Using the updated $\gamma$-ray angular distribution, the previous cross section results are in good agreement with reference data.

**PACS.** 25.40.Fq Inelastic neutron scattering – 23.20.En Angular distribution and correlation measurements

## 1 Introduction

The nuclide $^{56}$Fe has been included in the recent CIELO international nuclear data evaluation [1] since it is an important structural material in both nuclear engineering and nuclear physics research applications. Due to its relevance for the development and neutronic simulations for innovative fast reactor systems, the inelastic scattering cross section of $^{56}$Fe is part of the High Priority Request List of OECD/NEA [2].

Recently, a high-resolution measurement of the inelastic scattering cross section was done at JRC-Geel [3]. Neutron differential cross sections were previously measured at University of Kentucky from 1.3 to 7.96 MeV at angles from 30° to 154° and the angle integrated cross section was determined with an energy resolution between 80 to 170 keV [4].

The neutron induced cross sections of $^{56}$Fe exhibit significant fluctuations that extend from the respective threshold up to energies above 5 MeV. Extending the resolved resonance range in the data evaluation requires high energy-resolution data. Even in the range where the resonances start to strongly overlap the excitation functions still exhibit strong variations if they are measured with sufficiently high resolution. These Ericson fluctuations can be traced back to chaotic scattering in the regime of strongly overlapping resonances and can be explained by random-matrix theory [5]. The compound-nucleus cross sections fluctuate as do the angular distributions of the emitted particles and $\gamma$-rays. The fluctuations have the same magnitude as the average cross section. This fact can be used to measure the average width of the compound resonances which for the mass A=60 region might amount to about 10 keV [6].

The recent high-resolution measurement at JRC-Geel was mostly independent of the angular distribution of the $\gamma$-rays. The high-purity germanium (HPGe) detectors were positioned under 110° and 150°, where the Legendre polynomial $P_4$ vanishes. This enables the determination of the angle integrated $\gamma$-ray production cross section almost independently of the angular distribution [7].

The angular distribution of 847 keV $\gamma$-rays from inelastic neutron scattering from $^{56}$Fe has been measured before

[a] e-mail: roland.beyer@hzdr.de
[b] *Present address:* The University of Edinburgh, Edinburgh EH8 9YL, United Kingdom
[c] *Present address:* Los Alamos National Laboratory, Los Alamos, NM 87545, USA
[d] *Present address:* National Superconducting Cyclotron Laboratory, Michigan State University, East Lansing, MI 48824, USA

at the Argonne Fast Neutron Generator [8], where a single Ge(Li) detector was used under different angles. The sample sizes were rather large (cylinders with diam.×height of 2 cm×2 cm and 3.8 cm×3.8 cm) and the energy resolution due to the quasi mono-energetic neutron source was about 65 keV. Variations in the $\gamma$-ray angular distribution near threshold and decreasing anisotropy with increasing neutron energy was found.

Furthermore there is also a high-resolution measurement of the same angular distribution from ORELA, Oak Ridge, up to a neutron energy of 2100 keV using NE213 liquid scintillators for $\gamma$-ray detection under 30°, 90° and 125° [9]. The $\gamma$-ray angular distributions from this work however is not included in the EXFOR [10] nuclear data base.

## 2 Previous cross section measurement

In a previously published work the cross section for inelastic scattering of fast neutrons from excited states in $^{56}$Fe was determined using a single HPGe detector [11]. This detector was placed at an angle of $\theta = 125°$ relative to the incoming neutron beam and was used to measure the photon yield $N_{\mathrm{det}}(E_\gamma)$ for the emission of a certain $\gamma$-ray energy $E_\gamma$. The angle integrated $\gamma$-ray production cross section $\sigma_{E_\gamma}$ was extracted via the relation:

$$\sigma_{E_\gamma} = \frac{N_{\mathrm{det}} \cdot (1 - p_{\mathrm{mult}})}{\varepsilon_\gamma \cdot f_{\mathrm{trans},\gamma} \cdot W(\theta)} \cdot \frac{1}{\Phi_{\mathrm{n}} \cdot f_{\mathrm{trans,n}} \cdot A_{\mathrm{targ}}} \cdot \frac{1}{N_{\text{Fe-56}}} \qquad (1)$$

where $p_{\mathrm{mult}}$, $f_{\mathrm{trans},\gamma}$ and $f_{\mathrm{trans,n}}$ are correction factors accounting for multiple scattering, $\gamma$-ray transmission out of the sample and neutron transmission into the sample, respectively. $\varepsilon_\gamma$ is the $\gamma$-ray full energy detection efficiency, $\Phi_{\mathrm{n}}$ is the incoming neutron fluence, $A_{\mathrm{targ}}$ the geometrical cross section of the sample and $N_{\text{Fe-56}}$ the number of $^{56}$Fe nuclei in the sample. See ref. [11] for details. The angular distribution factor $W(\theta)$ was assumed to be unity over the whole neutron energy range, because the Legendre polynomial $P_2$ vanishes at $\theta = 125°$ and no significant data with sufficient resolution was available for higher order contributions. At the end an average deviation of about 10 % from evaluated and previuosly measured data was found, that might be caused by this rough assumption. Therefore, a new measurement of the $W(\theta)$ with high neutron energy resolution was performed at the *n*ELBE neutron time-of-flight facility and is reported here.

From eq. (1) one can see that the properties of the neutron beam and the sample cancel out when calculating the cross section ratio:

$$\frac{\sigma(\theta)}{\sigma(90°)} = \frac{N_{\mathrm{det}}(\theta) \cdot f_{\mathrm{corr}}(\theta)}{W(\theta)} \cdot \frac{W(90°)}{N_{\mathrm{det}}(90°) \cdot f_{\mathrm{corr}}(90°)} \qquad (2)$$

The correction factors $f_{\mathrm{corr}}(\theta)$ combine all corrections, which are different for the individual detectors, *i.e.* efficiency, and $\gamma$-ray absorption. The angle-integrated $\gamma$-ray production cross section should be independent of the detector position, *i.e.* $\frac{\sigma(\theta)}{\sigma(90°)} \equiv 1$. Therefore, one can define and determine the normalized angular distribution $W_{\mathrm{n}}(\theta)$ by:

$$W_{\mathrm{n}}(\theta) := \frac{W(\theta)}{W(90°)} = \frac{N_{\mathrm{det}}(\theta) \cdot f_{\mathrm{corr}}(\theta)}{N_{\mathrm{det}}(90°) \cdot f_{\mathrm{corr}}(90°)} \qquad (3)$$

The angular distribution $W(\theta)$ can be expressed in Legendre polynomials,

$$W(\theta) = 1 + a_2 P_2(\cos\theta) + a_4 P_4(\cos\theta) + \cdots \qquad (4)$$

Depending on the multipolarity of the observed $\gamma$-rays it is sufficient to use a maximum polynomial order of only 4 to describe the experimental data. From eq. (4) the following expression for $W_{\mathrm{n}}$ can be derived:

$$W_{\mathrm{n}}(\theta) = \frac{1 + a_2 P_2(\cos\theta) + a_4 P_4(\cos\theta)}{1 + a_2 \underbrace{P_2(\cos 90°)}_{=-0.5} + a_4 \underbrace{P_4(\cos 90°)}_{=0.375}} \qquad (5)$$

This function can be used to fit the experimental results to determine the parameters $a_2$ and $a_4$.

## 3 The *n*ELBE neutron time-of-flight facility

The neutron time-of-flight (ToF) facility *n*ELBE is the first photo-neutron source at a superconducting electron accelerator. It exhibits a very precise time structure of the neutron pulses and also favorable background conditions due to the low instantaneous neutron flux and the absence of almost any moderating materials. At *n*ELBE an electron beam of 30 MeV kinetic energy is focused onto a liquid lead target to produce bremsstrahlung that subsequently produces neutrons via photo-nuclear reactions on the lead nuclei. The short (5 ps) micropulse length and variable continuous-wave repetition rate (typically between 25 and 400 kHz) of the electron beam of the ELBE accelerator [12,13] together with a very compact neutrons-producing target (thickness 11 mm) [14,15] allows using a short flight path (5 to 11 m) and a correspondingly high neutron intensity. With such a neutrons-producing target the energy resolution in the fast neutron range is dominated by the achievable time resolution of the detectors used. The response functions of different neutron ToF facilities are discussed in detail in the review article by Schillebeeckx *et al.* [16].

The *n*ELBE neutron spectrum ranges from ca. 10 keV up to 10 MeV. The source strength is typically around $2 \cdot 10^{11}$ n/s which scales down to a neutron flux of approximately $3 \cdot 10^4$ n/cm$^2$/s at the sample position. Further properties of the *n*ELBE neutron beam are described in detail in ref. [17]. A schematic view of the *n*ELBE facility is shown in fig. 1.

## 4 Experimental setup

For the present experiment a kinetic energy of 30 MeV, a repetition rate of 101.6 kHz and a bunch charge of 46 pC,

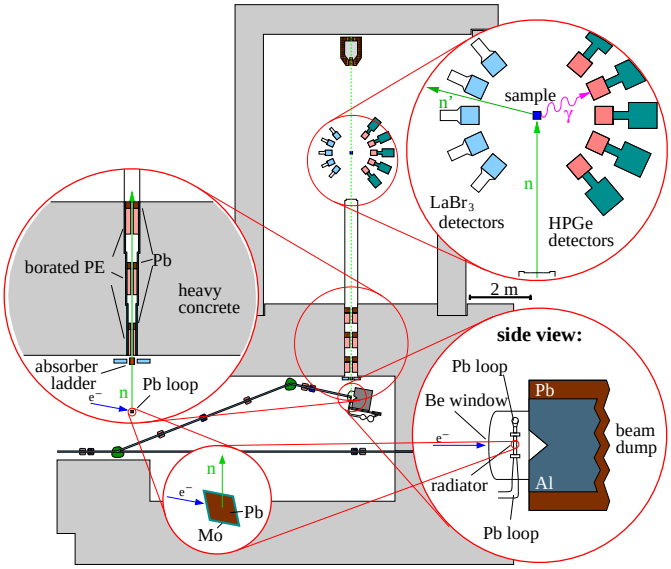


**Fig. 1.** Schematic floorplan of the *n*ELBE neutron time of flight facility and the detector setup for angular distribution measurements. The sample is surounded by five $LaBr_3$ and five HPGe detectors placed at angles of 30°, 55°, 90°, 125° and 150° with respect to the incoming neutron beam. See text for details.

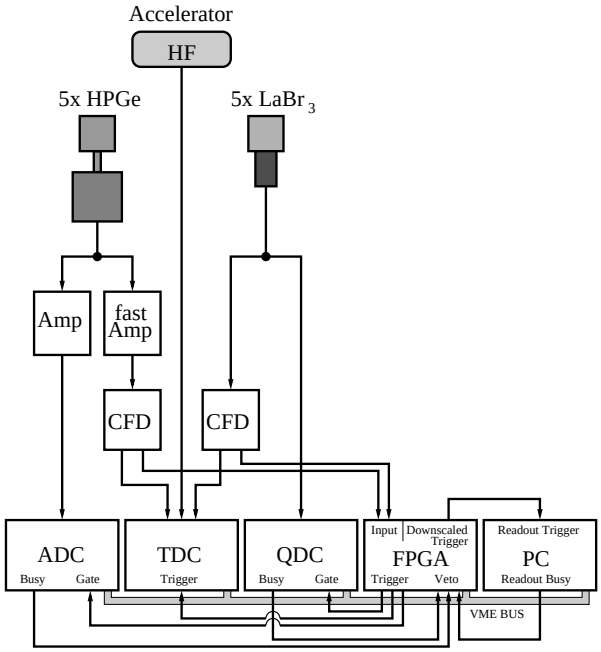


**Fig. 2.** Schematic view of the data acquisition electronics. See text for details.

*i.e.* an average beam current of 4.7 $\mu$A, were chosen for the ELBE electron beam parameters.

The sample was a cylindrical disk of natural iron with 4.5 mm thickness, 79 mm diameter and a mass of 172.1 g. It was positioned at a flight path of 830 cm. A tilt of 19.5° between the normal of the sample front face and the beam axis was included to prevent the detectors placed at 90° from pointing perpendicular onto the lateral surface of the sample. Around the sample five $LaBr_3$ scintillation detectors and five HPGe detectors were arranged in a horizontal plane at distances of 30 cm between sample center point and detector front face. A schematic view of the detector setup is shown in fig. 1.

The $LaBr_3$ scintillators[1] were cylindrically shaped. One of the scintillators was 2" in diameter and 2" in thickness and was mounted at 30° with respect to the incoming neutron beam. The remaining four scintillators were 3" in diameter and 3" in thickness and mounted at 55°, 90°, 125° and 150°, respectively. Opposite to the beam axis, five cylindrical HPGe detectors[2] were located at the same angles. Four of the HPGe detectors were about 79 mm in diameter and 89 mm in thickness each (*i.e.* 100 % relative efficiency), the one at 30° was 68 mm in diameter and 77 mm in thickness (*i.e.* 60 % relative efficiency).

The list mode data acquisition system consisted of NIM analog and VME digital electronics, measuring time and energy information for each single detector. An electronics schema is shown in fig. 2. The detector output signals are split into two signal paths: a timing and an energy branch. In the energy branch the signals of the HPGe detector are amplified and shaped by spectroscopic amplifiers[3] and feed into an 8-channel 32-event 12-bit peak-sensing analog-to-digital converter (ADC)[4]. The timing branch consists of a fast amplifier[5], constant fraction discriminators (CFD)[6] and a 32-channel multi-event multi-hit time-to-digital converter (TDC)[7]. This TDC digitizes all incoming signals in a free-running mode into a temporary buffer. When it gets a trigger signal it writes all hits of all detectors inside a pre-defined time interval (match window), even those that occurred before the trigger, into its output buffer. To enable the time-of-flight measurement the high-frequency (HF) reference signal of the accelerator is also fed into the TDC.

The signals emitted by the $LaBr_3$ detectors are rather short and intense with rise (fall) times of 1 to 2 ns (10 to 20 ns) and amplitudes up to a few volts. Therefore, they don't need further amplification and shaping. For them the energy branch reduces to an 8-channel 32-event charge-to-digital converter (QDC)[8] and the timing branch to CFDs and the same TDC as for the HPGe detectors.

The CFD signals are also used for trigger production via a field programmable gate array (FPGA) housed by a multi-purpose logic VME module[9]. This FPGA module creates the logical OR of all detectors to produce the gate signals for the ADC and the QDC and the trigger for the TDC. Furthermore it reads back the busy signals from the

[1] Saint-Gobain Crystals, Type Brillance 380
[2] 3× Ortec, 2× CANBERRA Industries Inc.
[3] Ortec 671
[4] CAEN V1785N
[5] Ortec 474
[6] in-house development
[7] CAEN V1290A
[8] CAEN V965A
[9] CAEN V1495

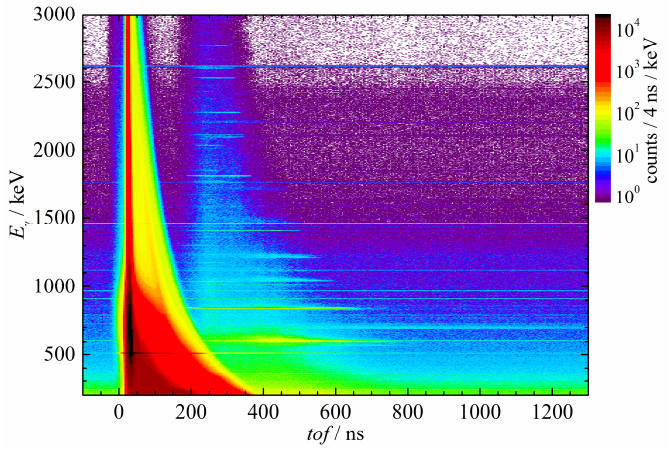


**Fig. 3.** Time-of-flight and $\gamma$-ray energy correlation measured by the HPGe detector located at an angle of 55°.

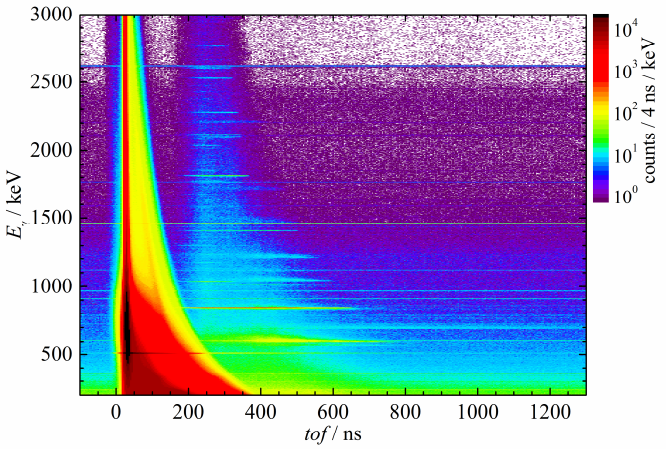


**Fig. 4.** Time-of-flight and $\gamma$-ray energy correlation measured by the $LaBr_3$ detector located at an angle of 55°.

ADC and QDC to produce a veto signal to inhibit trigger production while these modules are converting data. The length of the veto signal of each trigger event is saved into a FIFO buffer to enable an event-wise dead time correction. After 32 events are recorded the FPGA sends a readout trigger to the VME PC[10] that reads out the data from the buffers of TDC, ADC and QDC and writes them into list-mode data files at a network data server.

## 5 Data analysis

Figs. 3 and 4 show spectra taken with the experimental setup and conditions described in the previous section. Examples of $\gamma$-ray energy $E_\gamma$ versus neutron time-of-flight *tof* spectra for one HPGe and one $LaBr_3$ detector are shown. The energy and efficiency calibration was done using calibrated point sources of $^{137}$Cs, $^{60}$Co, $^{226}$Ra and $^{88}$Y. The time-of-flight calibration was done using the position of the photon flash $ch_\gamma$ (determined by fitting a Gaussian peak function), the known flight path $l$ (830 cm), the dispersion $d$ of the TDC (24.41 ps/channel) and the speed of light $c$ by means of the following relation:

$$tof = (ch - ch_\gamma) \cdot d + l/c. \qquad (6)$$

The photon flash is caused by the bremsstrahlung emitted from the neutrons-producing target. In figs. 3 and 4 the photon flash appears as vertical lines at a *tof* of about 28 ns and illustrates the different timing properties of the two detector types. The $LaBr_3$ detectors show a very sharp line over the complete $\gamma$-ray energy range whereas the HPGe detectors develop a large tailing especially at low $\gamma$-ray energies. This behaviour is directly correlated to the shape of the detector's output signals. The signals caused by scintillation light of the $LaBr_3$ detectors have an approximately constant shape, *i.e.* rise and fall time are independent of the pulse height, whereas the HPGe detectors develop signals whose rise times vary strongly due to the different charge collection times depending on the position of $\gamma$-ray interaction in the HPGe crystal. Conventional analog electronics is not capable to correct for this behaviour, which results in the limited time resolution and the tailing visible in the *tof*-spectrum.

As the electron bunch length of ELBE amounts to only a few ps, the width of the photon flash is given by the time resolution of the particular detector. From fitting the photon flash with a Gaussian peak function, the time resolution results in about 0.8 ns (FWHM) for the $LaBr_3$ and about 10 ns for the HPGe detectors. With an uncertainty of about 4.4 cm for the employed flight path (defined by half of the thickness of both the neutron source and of the detectors) this results in a neutron energy resolution at 1 MeV, *i.e.* at a *tof* of 600 ns, of 10 and 35 keV, respectively.

While the timing properties of the $LaBr_3$ detectors are superior to the ones of the HPGe detector, the latter show much better $\gamma$-ray energy resolution. For the HPGe detectors single $\gamma$-rays, *e.g.* the $^{40}$K line at 1461 keV, are visible as sharp horizontal lines (cf. fig. 3), while for $LaBr_3$ these lines appear as broad bands. For the $\gamma$-ray line at 1173 keV from a $^{60}$Co calibration source, the HPGe detectors show a resolution of 3.5 to 4.6 keV (FWHM) and the $LaBr_3$ detectors 34 to 41 keV.

Nevertheless, the $\gamma$-ray angular distribution can be extracted from both detector types. Five $\gamma$-ray transitions observed in this experiment were analyzed. They are listed in table 1. The 1408 keV transition of $^{54}$Fe could only be analyzed in the HPGe detector data due to the closeby $\gamma$-ray line from the decay of $^{40}$K at 1461 keV leading to overlapping peaks in the $LaBr_3$ histograms.

The first steps of data analysis were a *tof*-dependent dead time correction according to the description in ref. [17] and a background correction via subtraction of spectra taken with identical experimental conditions but removed sample. Afterwards the 2D *tof*-$E_\gamma$-histograms within certain *tof* intervals, *i.e.* neutron energy intervals, were projected onto the $E_\gamma$-axis. For the $LaBr_3$ detectors the

[10] CES RIO4-8072

**Table 1.** Parameters of the $\gamma$-ray transitions observed and analyzed in this work. Uncertainties can be found in refs. [18, 19].

| $E_\gamma$ / keV | initial state $J^\pi$,$E_\mathrm{i}$ / keV | final state $J^\pi$,$E_\mathrm{f}$ / keV | Multi-polarity |
|---|---|---|---|
| $^{56}$Fe: | | | |
| 847 | $2^+$, 846.78 | $0^+$, 0 (G.S.) | E2 |
| 1238 | $4^+$, 2085.10 | $2^+$, 846.78 | E2 |
| 1811 | $2^+$, 2657.59 | $2^+$, 846.78 | M1+E2 |
| 1038 | $4^+$, 3122.97 | $4^+$, 2085.10 | M1(+E1) |
| $^{54}$Fe: | | | |
| 1408 | $2^+$, 1408.19 | $0^+$, 0 (G.S.) | E2 |

*tof* intervals were chosen to have a width of 2 ns for the most prominent transition at 847 keV and 10 ns for the others. For the HPGe detectors *tof* intervals of 10 ns were taken for all transitions. The peaks in the resulting $\gamma$-ray energy histograms were fitted by Gaussian peak functions plus a linear function to account for the local background level. The fitted peak area gives the yield $N_\mathrm{det}(\theta, E_\gamma, \Delta E_\mathrm{n})$ of $\gamma$-rays with energy $E_\gamma$ produced by neutrons in the energy interval $\Delta E_\mathrm{n}$ at an emission angle $\theta$ with respect to the incoming neutron beam. For clarity reasons the dependency on $E_\gamma$ and $\Delta E_\mathrm{n}$ will no longer be explicitly mentioned in the following discussion.

From the yield $N_\mathrm{det}(\theta)$ the normalized angular distribution $W_\mathrm{n}(\theta)$ can be calculated using eq. (3). Therefore, the correction factors $f_\mathrm{corr}$ have to be determined, *i.e.* detection efficiency $\varepsilon$ and $\gamma$-ray absorption in the sample.

The sample is a flat disk of 79 mm diameter and consequently has a different solid angle relative to the $\gamma$-ray detectors than the point-like calibration sources. Simulations using the Monte-Carlo particle transport code GEANT4[11] [20] were performed to determine the efficiency ratio $\varepsilon_\mathrm{ext}/\varepsilon_\mathrm{point}$ to take the difference between the calibration measurement and the experiment with a geometrically extended sample into account.

It turned out that the extended source efficiency is not very different from point sources. $\varepsilon_\mathrm{ext}/\varepsilon_\mathrm{point}$ is in the range between 0.989 and 1.005 depending on the detector position and size (cf. table 2).

The absorption of neutrons and of $\gamma$-rays inside the sample has also been determined using GEANT4 simulations. Due to the attenuation of the neutron flux, about 5 % less inelastic scattering events happen at the rear side of the sample compared to the front side. This effect on the neutron flux cancels out when calculating $W_\mathrm{n}(\theta)$ but slightly influences the mean flight path of $\gamma$-rays inside the sample. Between 11 and 32 % of the 847 keV $\gamma$-rays are absorbed or scattered away on their path from the point of creation to the detectors depending on the observation angle. This amount decreases for the higher $\gamma$-ray energies. In table 2 examples for the above mentioned correction factors are listed.

[11] GEANT4 was used in version 10.2 patch 2 with G4NDL4.5 data files and physics list QGSP_BIC_HP 2.0.

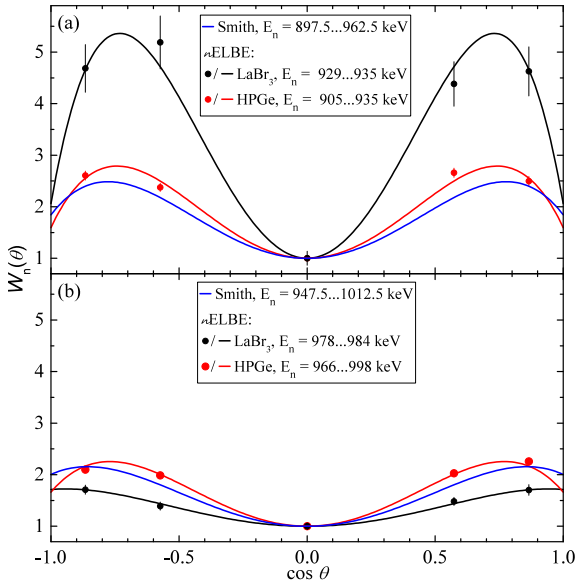


**Fig. 5.** Measured (dots) and fitted (lines) $\gamma$-ray angular distribution of the $E_\gamma = 847$ keV transition of $^{56}$Fe at $E_\mathrm{n} \approx 930$ keV (a) and $E_\mathrm{n} \approx 980$ keV (b) compared to the data of Smith [8] (blue line).

In the end, $W_\mathrm{n}(\theta)$ can be determined using the $N_\mathrm{det}(\theta)$ and the corrections mentioned above. Fig. 5 shows examples of the angular distribution of the 847 keV $\gamma$-rays from $^{56}$Fe. For these plots two neighboring neutron energy intervals around 930 and 980 keV also used before by Smith [8] were chosen. The quasi monoenergetic neutron spectra used by Smith definded an interval width of 65 keV for his data. The ToF intervals of 2 ns and 10 ns set in the analysis of the $LaBr_3$ and HPGe detector data, respectively, correspond to 6 keV and 30 keV wide bins at these energies. Therefore the neutron-energy resolution of the HPGe detector data is comparable with that of Smith but the $LaBr_3$ results are more detailed. As one can see in fig. 5 the HPGe detector data are consistent with the Smith data, while the $LaBr_3$ data reveal strong fluctuations with energy. This gets even more visible when one determines the angular distribution coefficients $a_2$ and $a_4$ by fitting the function given by eq. (5) to the measured points. These fitted curves are shown in fig. 5 as solid lines.

## 6 Results

In fig. 6 the resulting angular distribution coefficients of the 847 keV $\gamma$-rays are plotted over the whole energy range covered by the *n*ELBE neutron spectrum. The comparison with the data by Smith [8] and also Benjamin *et al.* [21] shows good aggreement with both *n*ELBE data sets. The HPGe detector data exhibit an energy resolution comparable to the Smith data, while the $LaBr_3$ data reveal more details especially in the region below 2 MeV. The $a_2$ value is clearly positive and $a_4$ mainly negative as expected for a $2^+ \rightarrow 0^+$ E2 transition. Above 2 MeV the angular distribution flattens out. This is mainly caused by the in-

**Table 2.** Correction factors for the different detectors. The $\gamma$-ray detection efficiency $\varepsilon_\gamma$, the efficiency ratio between an extended and a point-like calibration source $\varepsilon_{\rm ext}/\varepsilon_{\rm point}$ and the $\gamma$-ray transmission $f_{trans,\gamma}$ through the sample are tabulated for all detectors for the case of the 847 keV $\gamma$-ray from the de-excitation of the first excited state of $^{56}$Fe.

| HPGe | 30° | 55° | 90° | 125° | 150° |
|---|---|---|---|---|---|
| $\varepsilon_\gamma/10^{-5}$ | 0.73(2) | 1.18(2) | 1.05(2) | 1.15(2) | 1.12(2) |
| $\varepsilon_{\rm ext}/\varepsilon_{\rm point}$ | 0.9979(8) | 1.0045(7) | 1.0028(7) | 0.9942(7) | 0.9893(7) |
| $f_{trans,\gamma}$ | 0.8430(7) | 0.6849(5) | 0.7328(6) | 0.8698(6) | 0.8893(6) |
| **LaBr$_3$** | **30°** | **55°** | **90°** | **125°** | **150°** |
| $\varepsilon_\gamma/10^{-5}$ | 0.49(1) | 1.58(3) | 1.52(3) | 1.53(3) | 1.56(3) |
| $\varepsilon_{\rm ext}/\varepsilon_{\rm point}$ | 0.9945(11) | 0.9943(7) | 1.0048(7) | 1.0041(7) | 0.9989(7) |
| $f_{trans,\gamma}$ | 0.8892(9) | 0.8685(7) | 0.7321(6) | 0.6860(6) | 0.8431(6) |

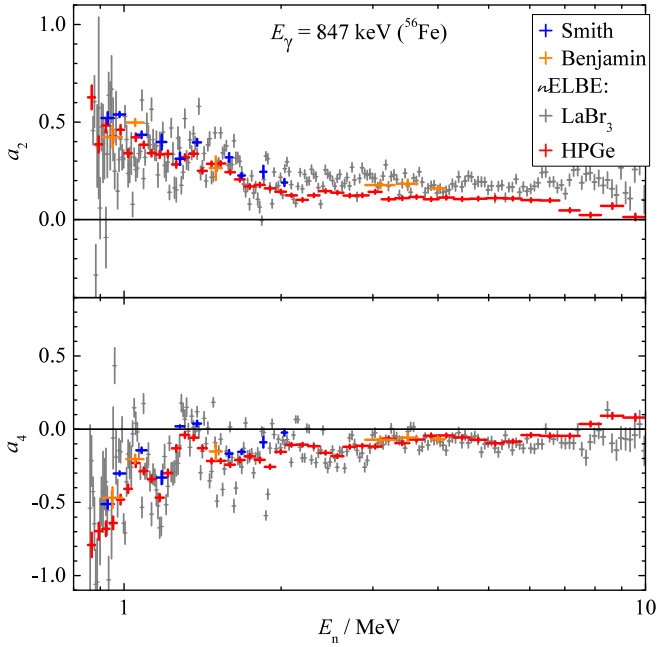


**Fig. 6.** Angular distribution coefficients $a_2$ and $a_4$ of the 847 keV $2^+ \rightarrow 0^+$ transition of $^{56}$Fe. The *n*ELBE data are compared to previous measurements by Smith [8] and Benjamin [21].

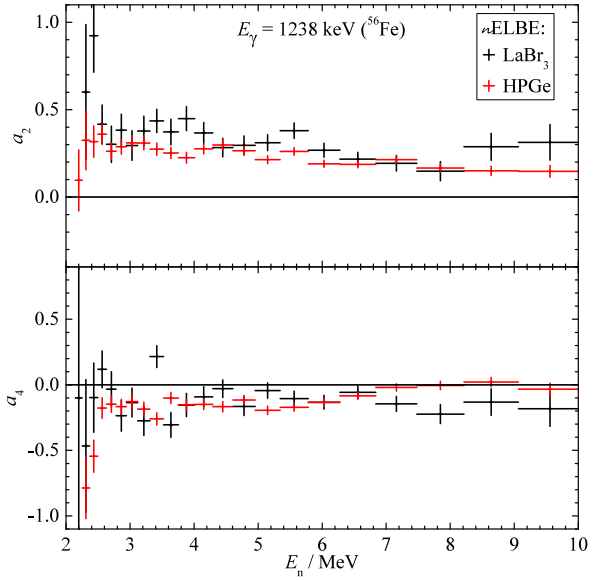


**Fig. 7.** Angular distribution coefficients $a_2$ and $a_4$ of the 1238 keV $4^+ \rightarrow 2^+$ transition of $^{56}$Fe.

creasing contribution of feeding transitions from higher states disturbing the spin orientation defined by the incoming neutron. Nevertheless, a positive $a_2$ value as well as a small negative $a_4$ component remain up to the end of the energy range investigated.

Figs. 7 to 9 show the angular distribution coefficients for the transition from higher states of $^{56}$Fe. For these transistion no data could be found in the literature to compare with. Due to lower statistics caused by the lower cross section and the decreasing incoming neutron flux above 2 MeV, these values had to be determined within larger *tof* bins and therefore with poorer energy resolution. Except for the region close to the thresholds, these transitions show rather constant angular distributions over the whole energy range. The 1238 keV transition shows positive $a_2$ and negative $a_4$ as it is a stretched E2 transition, while the 1811 keV M1+E2 mixed transition between equal spins is almost isotropic. The uncertainties of $a_2$ and $a_4$ for the 1038 keV transition are too large to assign a certain multipolarity but the values are compatible with the known assignment of M1(+E2).

In fig. 10 the angular distribution coefficients for the transition from the first excited state of $^{54}$Fe are plotted. The comparison to the few existing data points by Benjamin *et al.* [22] and Guenther *et al.* [23] shows a good agreement. However, the wider energy range covered by the present work reveals much more structure. Qualitatively the angular distribution of the 1408 keV $\gamma$-rays of $^{54}$Fe is similar to the one of the 847 keV $\gamma$-rays of $^{56}$Fe, which was expected, because both are $2^+ \rightarrow 0^+$ transitions.

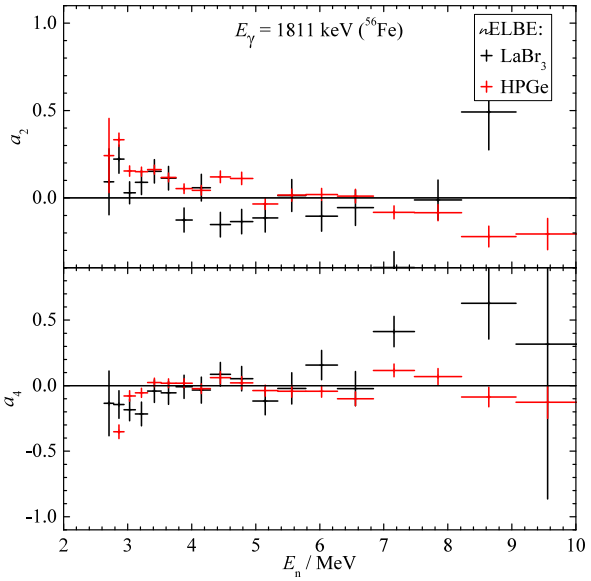


**Fig. 8.** Angular distribution coefficients $a_2$ and $a_4$ of the 1811 keV $2^+ \rightarrow 2^+$ transition of $^{56}$Fe.

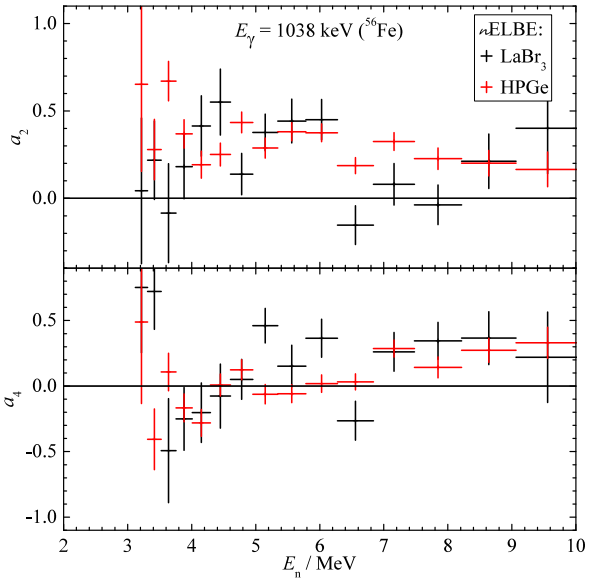


**Fig. 9.** Angular distribution coefficients $a_2$ and $a_4$ of the 1038 keV $4^+ \rightarrow 4^+$ transition of $^{56}$Fe.

## 7 Application to previous cross section measurement

Using the results for the angular distribution the cross section data determined in the $\gamma$-ray production measurement mentioned in sect. 2 and published in ref. [11] can be corrected for angular distribution effects. In that previous work an isotropic $\gamma$-ray distribution, *i.e.* $W(\theta) = 1$, was assumed due to a lack of precise data. Now the expression of eq. (4) for $\theta = 125°$ with the coefficients $a_2$ and $a_4$ determined in this work can be applied and inserted into eq. (1). In fig. 11 the result of this procedure is compared

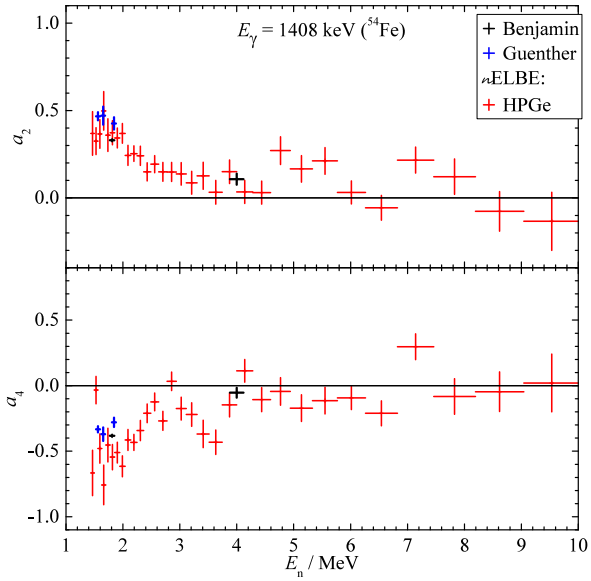


**Fig. 10.** Angular distribution coefficients $a_2$ and $a_4$ of the 1408 keV $2^+ \rightarrow 0^+$ transition of $^{54}$Fe. The *n*ELBE data are compared to previous measurements by Benjamin [22] and Guenther [23].

to the data obtained under the assumption of isotropic $\gamma$-ray emission. The angular correction causes a reduction of the cross section values by up to 30 %. One can see that the *n*ELBE data now agree very well with the data of Perey *et al.* [24] and Negret *et al.* [3]. The evaluated data files still show larger deviations of up to 20 % from all the measurements.

## 8 Summary

The angular distribution of $\gamma$-rays emitted during neutron inelastic scattering from a natural iron sample has been determined in the energy range from the reaction threshold up to 10 MeV at the *n*ELBE neutron time-of-flight facility. Two different sets of detectors, namely five HPGe and five $LaBr_3$ detectors, have been used to obtain data with different energy and time resolution. The $\gamma$-ray yields of five different nuclear transitions of $^{56}$Fe and $^{54}$Fe (see table 1) have been measured at 30°, 55°, 90°, 125° and 150° relative to the incoming neutron beam. From these yields the normalized angular distribution $W_n(\theta, E_\gamma, E_n)$ has been calculated taking corrections for the data acquisition dead time, the $\gamma$-ray detection efficiency, and the neutron and $\gamma$-ray absorption in the sample into account. By fitting $W_n(\theta, E_\gamma)$ at a certain neutron energy $E_n$ by the ratio of two Legendre polynomials (see eq. (5)) the angular distribution coefficients $a_2$ and $a_4$ have been determined. The angular distribution coefficients for three transitions in $^{56}$Fe (1038, 1238 and 1811 keV) are reported here for the first time. The results for the $\gamma$-rays from the de-excitation of the first excited states in $^{54}$Fe and $^{56}$Fe are consistent with previously measured data but contribute knowledge over a much wider energy range. The high neutron-energy

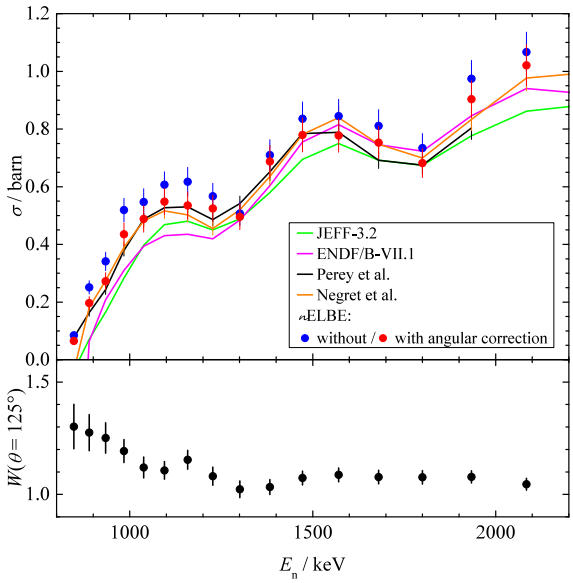


**Fig. 11.** Inelastic scattering cross section of $^{56}$Fe for the excitation of the first excited state ($E_x = 847$ keV). The previously published data [11] were corrected for the $\gamma$-ray angular distribution $W(\theta = 125°)$ using the results of the present work. For comparison the data measured by Perey *et al.* [24] and Negret *et al.* [3] and evaluated data from the JEFF [25] and ENDF [26] library are ploted. These reference data were smoothed to the same resolution as the *n*ELBE data.

resolution data taken with the $LaBr_3$ scintillators reveal a lot of structures that have not been visible before.

The results of this work have been used to correct a previously measured inelastic neutron scattering cross section (see ref. [11]) taken at 125° for the effect of the angular distribution. A correction of up to 30 % was calculated, bringing the data in good agreement with previously measured data sets. Since the Legendre polynomial $P_2$ vanishes at 125° this correction is caused only by the $a_4P_4$ term. This fact illustrates the necessity of taking angular distribution effects of higher orders into account. A measurement only at 125° might not be enough to determine angle integrated cross sections. As was already stated by others [7], further angles have to be considered, too.

We thank the staff of the ELBE accelerator for their valuable support during the experiments and A. Hartmann, K. Heidel and M. Görler for technical assistance. We also thank St. Gohl and L. Wagner for running shift during the beam time and, last but not least, Nik Kurz from GSI Darmstadt for his assistance during the development of the DAQ.

Part of this work was content of the master thesis of Mirco Dietz [27].

This work was supported by the European Commission within the 7$^{th}$ framework programme projects ERINDA (FP7-269499) and CHANDA (FP7-605203).

## References

1. The CIELO project, `https://ndclx4.bnl.gov/gf/project/cielo_iron/`
2. NEA Nuclear Data High Priority Request List, `https://www.oecd-nea.org/dbdata/hprl/`
3. A. Negret *et al.*, Phys. Rev. C **90** (2014) 034602
4. A.P.D. Ramirez *et al.*, Phys. Rev. C **95** (2017) 064605
5. G.E. Mitchell *et al.*, Rev. Mod. Phys. **82** (2010) 2845
6. K.A. Eberhardt *et al.*, Proc. Int. Conf. Stat. Prop. Nucl. 1971, Plenum Press, N.Y. (1972) 139
7. L.C. Mihailescu *et al.*, Nucl. Inst. Meth. A **531** (2004) 375
8. D.L. Smith, Report ANL/NDM-20 (1976)
9. W. Kinney *et al.*, Nucl. Sci. Eng. **63** (1977) 418
10. N. Otuka *et al.*, Nucl. Data Sheets **120** (2014) 272
11. R. Beyer *et al.*, Nucl. Phys. A **927** (2014) 41
12. F. Gabriel *et al.*, Nucl. Instr. Meth. B **161** (2000) 1143
13. J. Teichert *et al.*, Nucl. Instr. Meth. A **507** (2003) 354
14. E. Altstadt *et al.*, Ann. Nucl. Energy **34** (2007) 36
15. J. Klug *et al.*, Nucl. Instr. Meth. A **577** (2007) 641
16. P. Schillebeeckx *et al.*, Nucl. Data Sheets **113** (2012) 3054
17. R. Beyer *et al.*, Nucl. Instr. Meth. A **723** (2013) 151
18. H. Junde *et al.*, Nucl. Data Sheets **107** (2006) 1393
19. H. Junde *et al.*, Nucl. Data Sheets **112** (2011) 1513
20. S. Agostinelli *et al.*, Nucl. Instr. Meth. A **506** (2003) 250
21. R.W. Benjamin *et al.*, Nucl. Phys. **79** (1966) 241
22. R.W. Benjamin *et al.*, Phys. Rev. **163** (1967) 1252
23. P.T. Guenther *et al.*, Ann. Nucl. Energy **13** (1986) 601
24. F.G. Perey *et al.*, Proc. 3rd Int. Conf. Neutron Cross Sections Tech., Knoxville, TN, USA, (C,71 KNOX,1,197103) (1971) 191
25. JEFF-3.2 evaluated data library, `http://www.oecd-nea.org/dbforms/data/eva/evatapes/jeff_32/`
26. M.B. Chadwick *et al.*, Nucl. Data Sheets **112** (2011) 2887
27. M. Dietz, Master Thesis, Technische Universität Dresden, Germany (2016) `https://www.hzdr.de/publications/PublDoc-11136.pdf`